Chinese Chemical Letters 34 (2023) 107308

Contents lists available at ScienceDirect

Chinese Chemical Letters

journal homepage: www.elsevier.com/locate/cclet

# Construction of oxygen defective $ZnO/ZnFe_2O_4$ yolk-shell composite with photothermal effect for tetracycline degradation: Performance and mechanism insight

Ke Zhang, Hongyang Cao, Afzal Dar, Danqing Li, Lina Zhou, Chuanyi Wang*

*School of Environmental Science and Engineering, Shaanxi University of Science and Technology, Xi'an 710021, China*

ARTICLE INFO

*Article history:*
Received 3 January 2022
Revised 2 February 2022
Accepted 8 March 2022
Available online 11 March 2022

*Keywords:*
Photocatalysis
Photothermal
Oxygen vacancy
Yolk-shell
Tetracycline

ABSTRACT

Oxygen vacancy induced photothermal effect is of great significant but lack of adequate attentions for environmental remediation. In this paper, green recyclable $ZnO/ZnFe_2O_4$ with oxygen vacancy was prepared by a solvothermal-calcination method. The UV-vis light capture ability of $ZnO/ZnFe_2O_4$ microspheres is improved with the multiple light reflections due to the yolk-shell structure, and the oxygen vacancy expands the absorption range of photocatalyst and enhances photothermal conversion. The optimized photocatalyst can heat the solution from room temperature to 70 °C within 60 min of visible light illumination, and the light to heat conversion efficiency is achieved by 61.3%. Compared with the degradation efficiency at 20 °C, photothermal catalysis achieves a stable degradation in 80 min, and the degradation efficiency is increased by 41.5%. This can be attributed to the fact that light induced thermal energy accelerates the migration of electrons and holes, and promotes the diffusion of free radicals by heating active centers *in situ*. The active species contributing to the degradation, in order of importance, are the superoxide radical, hydroxyl radical, hole and electron. The light-to-thermal assisted photocatalysis with $ZnO/ZnFe_2O_4$ provides a new sight for the pollution control in the future practical applications.



As an effective antibiotic, tetracycline (TC) has been widely used in recent decades, which can interfere with cells and hinder their normal function [1,2]. Due to its stability in aqueous solution, TC is difficult to be eliminated by conventional treatment or biodegradation process, thus giving rise to significant potential hazards to human health and ecological balance. In recent years, many technologies, such as photocatalysis, adsorption and Fenton oxidation, have been used to treat TC pollution [3–8]. However, the adsorption method cannot degrade the TC, and the adsorbent often requires expensive and toxic solvents for regeneration, the regenerated liquid waste also requires additional treatment and disposal. Fenton technique requires oxidation reagent, and the deposition of large amounts of ferric ion sludge increase cost dramatically [9]. UV radiations and ultrasonic treatment have limited penetration power in the aqueous solution, and they are harmful to eyes and skin [10]. Among many technologies, photocatalysis has attracted much attention to purify industrial and culture wastewater because of its low cost and high efficiency [11,12]. Metal oxides such as ZnO and $ZnFe_2O_4$ have been widely used in photocatalysis due to their fast hole transport, underwater stability and high light absorption coefficient [13–16]. Therefore, we constructed $ZnO/ZnFe_2O_4$ nanocomposite with yolk-shell structure, which can not only provide large surface area, but also enhance the light absorbance as much as possible *via* multiple reflections inner the microsphere [17,18].

Surface reactive oxygen species (ROS) exhibit strong activity in the photodegradation of TC [19,20]. However, due to the high recombination of charge carrier, the existence of charge and energy transfer process, and the insufficient of dissolved oxygen in water after reaction, the ROS production is usually inefficient. If additional energy is supplemented, the reaction process will be continued and accelerate. Controlling the activation of oxygen is of great significance to achieve efficient and stable ROS generation. Direct conversion of solar energy into heat to drive oxygen activation is a new and effective way to utilize solar energy. However, most semiconductors only absorb ultraviolet light or part of visible light, how to effectively extend the light absorption range to convert long wavelength light into heat energy and improve the photocatalytic performance of the system is a challenging task.

Construction of oxygen vacancies is an effective way to enhance light adsorption and improve the separation efficiency of photogenerated carriers [21–24]. Currently, the wide usage of oxygen vacancy in photocatalysis is about the photoelectrons capture

* Corresponding author.
*E-mail address:* wangchuanyi@sust.edu.cn (C. Wang).

https://doi.org/10.1016/j.cclet.2022.03.031
1001-8417/

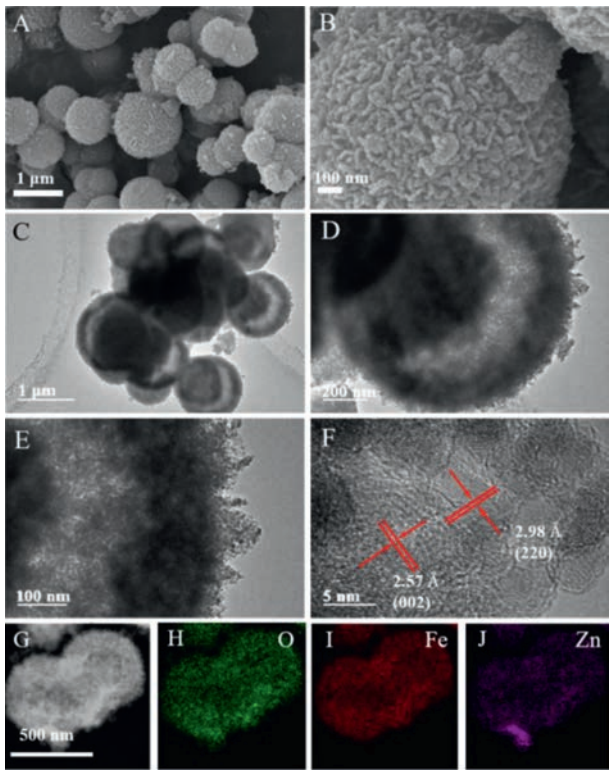


**Fig. 1.** (A, B) SEM images of $ZO_v/ZFO_v$ 500. (C–E) TEM images of $ZO_v/ZFO_v$ 500. (F) HRTEM image of an individual microsphere and (G–J) the corresponding elemental mapping images.

and light absorption extension. In fact, the oxygen vacancy induced photothermal effect may also be an important factor influencing photocatalytic process. In photocatalytic process, semiconductors with oxygen vacancies continuously generate heat energy, which affects the transport of photogenerated carriers and significantly improves the photocatalytic performance [25–27]. Additionally, evaporation of water by the photothermal effect can concentrate pollutant and achieve high removal efficiency [28]. But rare attention was devoted to the photothermal effect of oxygen vacancy during photodegradation process.

In this paper, $ZnO/ZnFe_2O_4$ with oxygen vacancy ($ZO_v/ZFO_v$) was synthesized by a solvothermal-calcination method. Detailed characterizations confirmed the yolk-shell $ZO_v/ZFO_v$ nanoparticles possess superior multi-reflection absorption capability. By optimizing the oxygen vacancy concentration to tune the optical absorption, $ZO_v/ZFO_v$ features outstanding TC degradation performance through photocatalysis coupled with photothermal effect. The influence of photothermal effect, possible mechanism and pathway of TC degradation on $ZO_v/ZFO_v$ were fully explored.

Scanning electron microscopy (SEM) and transmission electron microscopy (TEM) images of the as-prepared $ZO_v/ZFO_v$ 500 were recorded to characterize its morphologies. As shown in Figs. 1A and B, the sample exhibits sphere-like morphology with diameter of about 1 μm, consisting of small nanoparticles. Figs. 1C–E show that $ZO_v/ZFO_v$ 500 possesses a special yolk shell structure, and the average shell thickness as estimated from the histograms is $0.191 \pm 0.020$ μm (Fig. S3 in Supporting information). This special structure makes the microspheres inside have enough light scattering and multiple reflections to improve the light absorption and photothermal conversion. Fig. 1F displays the typical high resolution TEM image, and the spacing of lattice fringes is *ca.* 0.298 nm, corresponding to the (220) crystal plane of $ZnFe_2O_4$. Elemental mappings (Figs. 1G–J) exhibit the distribution of Zn, Fe, and O elements in $ZO_v/ZFO_v$ 500, demonstrating the nanocomposite with yolk-shell structure has been successfully prepared.

X-ray photoelectron spectroscopy (XPS) spectra was performed on $ZO_v/ZFO_v$ 500 to explore the surface chemical composition and chemical states. Survey spectrum in Fig. S6 (Supporting information) illustrates the prepared material contains O, Fe and Zn elements, further confirming the formation of $ZO_v/ZFO_v$ 500. The C 1s XPS spectrum could be deconvoluted into three peaks centered at 282.6, 284.0 and 286.4 eV, corresponding to C−C, C−O and C=O, respectively (Fig. S7A in Supporting information). In Fig. S7B (Supporting information), there are two binding energy peaks centered at 735.0 and 708.5 eV, corresponding to Fe $2p_{1/2}$ and Fe $2p_{3/2}$, respectively. XPS spectrum of Fe $2p_{3/2}$ could be fitted into 708.2 and 710.2 eV, belonging to tetrahedral and octahedral $Fe^{3+}$. Besides, the peak at 724 eV is consistent with the Fe $2p_{1/2}$ photoelectron response of $Fe^{3+}$. As shown in Fig. S7C (Supporting information), the high-resolution XPS spectra of Zn exhibits the binding energies of 1019.3 eV (Zn $2p_{3/2}$) and 1042.4 eV (Zn $2p_{1/2}$), indicating the presence of $Zn^{2+}$ in $ZO_v/ZFO_v$. According to the O 1s XPS spectrum (Fig. S7D in Supporting information), the three fitted binding energy peaks located at 531.0, 527.7 and 529.6 eV correspond to the adsorbed water, surface lattice oxygen of $ZFO_v$ and $ZO_v$, respectively [29].

Photothermal catalytic TC degradation was performed by using the as-prepared catalysts under visible light and near infrared (NIR) light. As shown in Fig. 2A, under visible light irradiation, $ZO_v/ZFO_v$ exhibited superior degradation efficiency, and the best degradation performance occurred in $ZO_v/ZFO_v$ 500. However, excessive defects will become new electron-hole recombination centers thus reducing the photocatalytic performance. As a result, $ZO_v/ZFO_v$ 600 exhibits worse activity than that of $ZO_v/ZFO_v$ 500. Fig. 2B shows the degradation rate constant of all the samples. The photodegradation rate constant of TC by $ZO_v/ZFO_v$ 500 (0.01650 $min^{-1}$) is 1.5 times and 14.1 times higher than that of $ZO_v$ (0.01118 $min^{-1}$) and $ZFO_v$ (0.001170 $min^{-1}$), indicating the superior performance of the nanocomposites. Temperature can increase the production rate of ROS and affect the catalytic activity. For comparison, as shown in Fig. S9 (Supporting information), TC cannot be degraded by visible light irradiation alone, and temperature has negligible impact on TC degradation. The performance of some photocatalysts for pharmaceutical personal care products' degradation is listed in Table S2 (Supporting information) [30–37]. To explore the temperature changes of the solution under light irradiation, temperature monitoring was carried out in TC degradation process with all the as-prepared samples. As shown in Fig. 2C, compared with ZO/ZFO, $ZO_v/ZFO_v$ exhibits better photo-thermal conversion capacity, and the best sample reaches equilibrium within 60 min, the light-to-heat conversion efficiency achieved 61.3%, suggesting that oxygen vacancy can more efficiently convert light energy into heat energy [38]. As shown in Figs. 2D–F, the catalysts under NIR irradiation exhibits a considerably worse photocatalytic performance and $\Delta T$ than the visible light irradiation, indicating the photocatalysis and photothermal conversion mainly rely on visible light.

The photothermal effect plays an important role in enhancing the photocatalytic degradation performance, and the diffuse reflection spectra (DRS) results indicate that $ZO_v/ZFO_v$ 500 has excellent absorption capability from visible light to NIR. Therefore, we explored the temperature changes of ZO/ZFO 500 and $ZO_v/ZFO_v$ 500 in visible and NIR by infrared thermal imager. As shown in Fig. S10A (Supporting information), at the initial time, the temperature of ZO/ZFO 500 is consistent with the room temperature. After turning on the lamp, the infrared image color of ZO/ZFO 500 became bright with the increase of time. After 16 min of illumination, the temperature rose to 73 °C, and then remained basi-

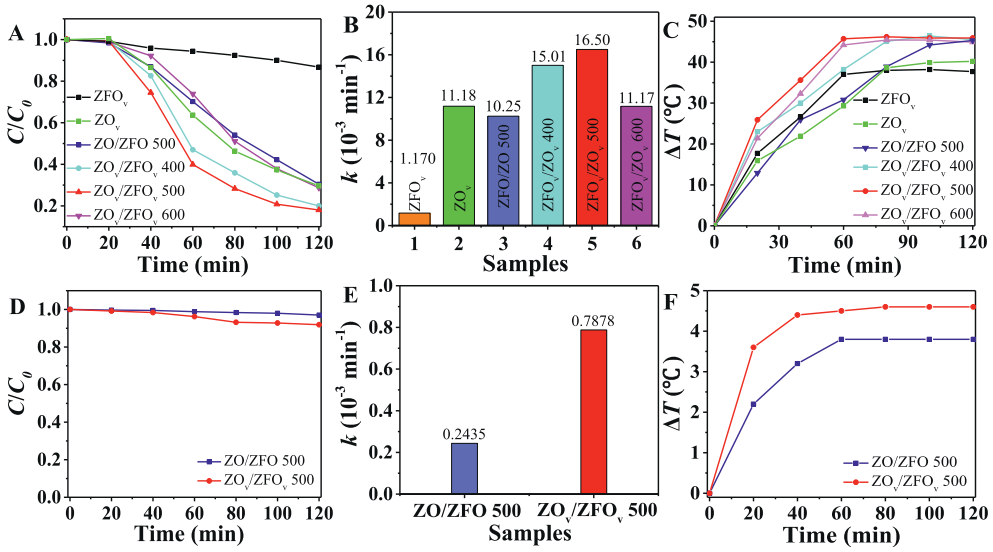


**Fig. 2.** Degradation performance (A), photodegradation rate constants (B) and $\Delta T$ (C) of $ZO_v/ZFO_v$ nanocomposite under visible light irradiation ($\lambda > 420$ nm, 0.29 W/cm$^2$) in water bath. Degradation performance (D), photodegradation rate constants (E) and $\Delta T$ (F) of $ZO_v/ZFO_v$ nanocomposite under NIR irradiation ($\lambda > 765$ nm, 0.07 W/cm$^2$).

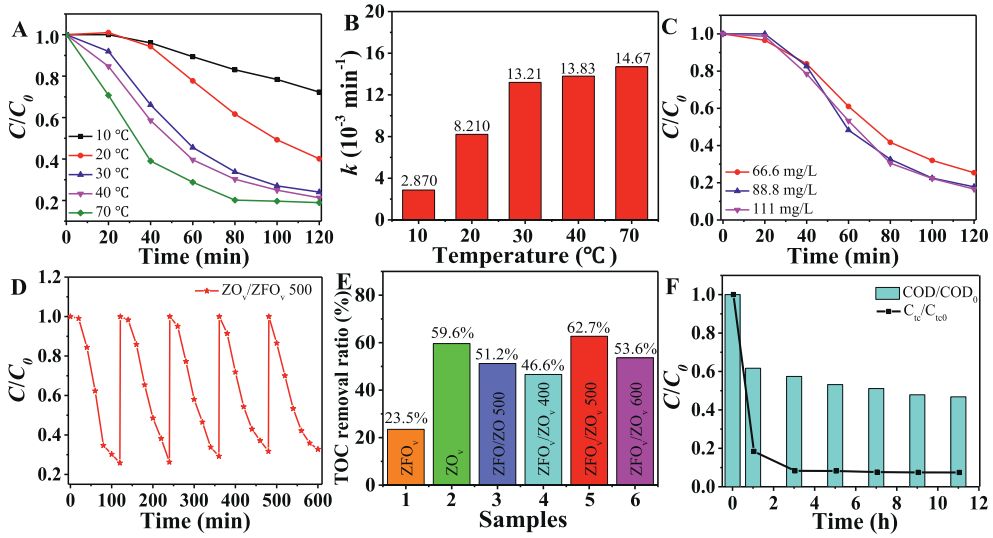


**Fig. 3.** Photodegradation performance (A) and degradation rate constants (B) of $ZO_v/ZFO_v$ 500 at different temperature. (C) Impact of TC concentration. (D) The cycling experiment for the degradation of TC by $ZO_v/ZFO_v$ 500. (E) TOC removal by all the as-prepared samples. (F) TC degradation and COD removal in real wastewater.

cally unchanged. Under the same irradiation condition, it can be seen from Fig. S10B (Supporting information) that the temperature of the $ZO_v/ZFO_v$ 500 nanocomposite increased to 72.1 °C within two minutes, and then continued to rise to 90.1 °C. As shown in Fig. S11 (Supporting information), ZO/ZFO 500 heats up slowly under NIR and the temperature is not high. The heating rate of $ZO_v/ZFO_v$ 500 under NIR is slightly faster than that of ZO/ZFO 500, and the result is consistent with those measured in solution. These experiments demonstrate that oxygen vacancy induced photothermal effect is mainly dependent on visible light rather than NIR.

As shown in Fig. 3A, temperature changes have significant impact on TC degradation. The TC degradation efficiency of $ZO_v/ZFO_v$ 500 at 10 °C, 20 °C, 30 °C, 40 °C and 70 °C are 27.7%, 59.9%, 76.0%, 78.7% and 81.5%, respectively, demonstrating that the higher temperature, the higher degradation efficiency. Combined with Fig. 2C, it can be analyzed that oxygen vacancy can improve the photothermal conversion efficiency, which is conducive to the photocatalytic degradation of TC. Fig. 3B shows the degradation rate constants of $ZO_v/ZFO_v$ 500 at different temperature, The rate of TC degradation reactions follows the Arrhenius law (Fig. S12 in Supporting information). As shown in Fig. 3C, photodegradation efficiency increases with the increase of TC concentration, and the degradation efficiency exhibits little change when the concentration reaches 111 mg/L. This result indicates that the catalyst also has a good removal effect on high concentration TC. As shown in Fig. 3D, the photocatalytic activity of $ZO_v/ZFO_v$ 500 remains 86.2% after 5 cycles, and XRD patterns demonstrate that the catalyst structure did not change after the test (Fig. S13 in Supporting information), suggesting $ZO_v/ZFO_v$ 500 has good stability. To further explore the mineralization ability of all samples towards TC, the total organic carbon (TOC) concentration was evaluated after photodegradation experiments. Fig. 3E shows that the TOC removal efficiency of $ZO_v/ZFO_v$ 500 is 62.7%. In order to explore the degradation performance of $ZO_v/ZFO_v$ 500 in the real waste water environment, the water sample from sewage treatment plant of Shaanxi University of Science and Technology was selected to carry out photocatalytic experiments. As shown in Fig. 3F, after 11 h of

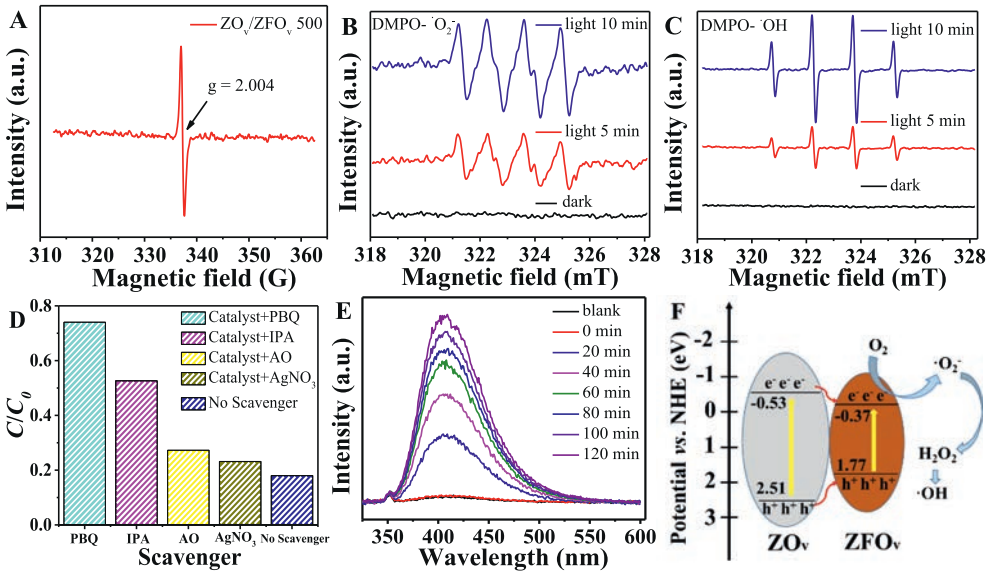


**Fig. 4.** (A) EPR plots of $ZO_v/ZFO_v$ 500. (B) DMPO spin-trapping EPR spectra for $^{\bullet}O_2^-$. (C) DMPO spin-trapping EPR spectra for $^{\bullet}OH$. (D) Active species quenching experiments over $ZO_v/ZFO_v$ 500. (E) Hydrogen peroxide trapping experiments of $ZO_v/ZFO_v$ 500. (F) Schematic of the possible carrier's separation process on the interface of $ZO_v/ZFO_v$ 500 under visible light irradiation.

visible light irradiation, the TC and chemical oxygen demand (COD) removal reaches *ca.* 92.6% and 53.2%, indicating that $ZO_v/ZFO_v$ 500 possesses great potential in practical application.

Electron paramagnetic resonance (EPR) was performed to verify the oxygen vacancy in $ZO_v/ZFO_v$ 500. As shown in Fig. 4A, $ZO_v/ZFO_v$ 500 displayed a symmetrical signal at $g = 2.004$, which can be attributed to the unpaired electrons on the oxygen vacancy sites, illustrating that $ZO_v/ZFO_v$ 500 was successfully synthesized. EPR was also carried out to confirm the existence of reactive oxygen species, which are produced under visible light in the process of photoreaction. As shown in Fig. 4B, no signal can be observed for $ZO_v/ZFO_v$ 500 in darkness. After irradiation, the signal with four peaks corresponding to $^{\bullet}O_2^-$ were appeared, and the intensity of this signal was enhanced with the extension of irradiation time. Similarly, the signal characteristics of the DMPO-$^{\bullet}$OH were also observed after irradiation (Fig. 4C).

In order to identify the main active species in degradation, active species trapping experiments were performed. Isopropyl alcohol (IPA), *p*-benzoquinone (PBQ), $AgNO_3$ and ammonium oxalate monohydrate (AO) were selected as the capture agent for $^{\bullet}OH$, $^{\bullet}O_2^-$, $e^-$ and $h^+$, respectively (Fig. 4D). The removal rate of TC reached 82.0% without any scavenger. After adding PBQ into the suspension, the TC degradation rate was dramatically decreased, indicating that $^{\bullet}O_2^-$ plays a significant role in the degradation process. The presence of IPA modestly inhibited the degradation, and the photocatalytic activity was only slightly inhibited after addition of AO and $AgNO_3$, respectively, demonstrating that $e^-$ and $h^+$ are inconsequential to TC degradation.

Combining with the results of Mott-Schottky (Fig. S5 in Supporting information) and DRS experiments (Fig. S4 in Supporting information), the nanocomposite cannot produce $^{\bullet}OH$ radicals through hole directly. In order to study whether the catalyst can produce $^{\bullet}OH$ radicals *via* $H_2O_2$ in the degradation process, the fluorescence intensity of $H_2O_2$ and its evolution with time were explored. As shown in Fig. 4E, the yield of $H_2O_2$ was gradually increased with the increase of time, proving that $^{\bullet}OH$ radicals were produced from $H_2O_2$.

According to the above discussion, a probable photocatalytic degradation mechanism was proposed in Fig. 4F. Because the conduction band (CB) of $ZO_v$ (−0.53 eV) is more negative than that of $ZFO_v$ (−0.37 eV), the excited electrons on $ZO_v$ could be transferred to the CB of $ZFO_v$ by electron injection. The electrons in $ZFO_v$ could react with surface adsorbed oxygen to form superoxide radicals, and parts of superoxide radicals further converted to hydrogen peroxide and thus generates hydroxyl radical to participate in degradation reaction. Because the valence band (VB) potential of $ZFO_v$ is more negative than the $OH^-/^{\bullet}OH$ potential, the positively charged holes in VB can only oxidize TC instead of oxidizing $H_2O$ or $OH^-$ to $^{\bullet}OH$.

The degradation intermediate products were analyzed by high performance liquid chromatograph-mass spectrometer (HPLC-MS) to investigate the photocatalytic pathways. Based on the HPLC-MS analysis, degradation and removal process can be divided into two main pathways (Fig. S14 in Supporting information). The first pathway is by the ring-opening reaction and the deprivation of methyl from the tertiary amine to generate the intermediate with *m/z* of 391.16 (**A1**), which is further fragmented to the product **A2** (*m/z* = 332.16) *via* the deprivation of amino group. Afterwards, the intermediates with the *m/z* values of 290.10 and 226.06 were degraded *via* the oxidation, dehydroxylation reaction, deethylation reaction and deacetylation reaction. Meanwhile, tetracycline was fragmented to **B1** (*m/z* = 360.15) by removal of the amide group, hydroxyl group and methyl. The intermediates with the *m/z* values of 316.16, 272.16, 261.17 and 245.18 are generated by the cleavage of specific functional groups and the ring-opening reactions. In the end, the intermediate products would be finally oxidized to $CO_2$, $H_2O$ and small inorganic molecules.

In conclusion, we successfully synthesized yolk-shell structure of $ZO_v/ZFO_v$ by a solvothermal-calcination method. The $ZO_v/ZFO_v$ catalyst with suitable oxygen vacancy concentration can effectively degrade TC under visible light irradiation. The superior photocatalytic performance of the nanocomposite can be ascribed to the following advantages: (1) Photothermal effect accelerates the migration of ROS and speeds up the reaction rate; (2) Oxygen vacancy and heterostructure extend the light absorption and improve the charge carriers' separation; (3) Yolk-shell structure leads to the superior multi-reflection absorption capability. The present work not only gives insights into the TC photodegradation by using $ZO_v/ZFO_v$, but also offers a solution to the practical application of photocatalysts in wastewater treatment.

## Declaration of competing interest

The authors declare that they have no known competing financial interests or personal relationships that could have appeared to influence the work reported in this paper.

## Acknowledgments

This work was supported by the National Natural Science Foundation of China (Nos. 21976116, 52161145409), Shaanxi Provincial Foreign Expert Project (No. 2021JZY-004), SAFEA of China (High-end Foreign Expert Project), Alexander-von-Humboldt Foundation of Germany (Group-Linkage Program), and the scientific research startup fund of Shaanxi University of Science and Technology.

## Supplementary materials

Supplementary material associated with this article can be found, in the online version, at doi:10.1016/j.cclet.2022.03.031.

## References

[1] J. Luo, X. Ning, L. Zhan, X. Zhou, Sep. Purif. Technol. 255 (2021) 117691.
[2] M. Abinaya, K. Govindan, M. Kalpana, et al., J. Hazard. Mater. 397 (2020) 122885.
[3] H. Qin, H. Cheng, H. Li, Y. Wang, Chem. Eng. J. 396 (2020) 125304.
[4] R. Hailili, Z. Wang, M. Xu, et al., J. Mater. Chem. A 5 (2017) 21275–21290.
[5] R. Hailili, Z. Wang, X. Gong, C. Wang, Appl. Catal. B: Environ. 254 (2019) 86–97.
[6] J. Wang, X. Yi, X. Xu, et al., Chem. Eng. J. 431 (2022) 133213.
[7] X. Zhang, F. Wang, C. Wang, et al., Chem. Eng. J. 426 (2021) 131927.
[8] H. Li, S. Sun, H. Ji, et al., Appl. Catal. B: Environ. 272 (2020) 118966.
[9] F. Li, Z. Wei, K. He, et al., Water Res. 185 (2020) 116219.
[10] A. Hafeez, F. Javed, T. Fazal, et al., Chem. Eng. Process. 159 (2021) 108205.
[11] Z. Xin, X. Zhao, H. Ji, et al., Chin. Chem. Lett. 32 (2021) 2151–2154.
[12] H. Sun, F. Guo, J. Pan, et al., Chem. Eng. J. 406 (2021) 126844.
[13] D. Kim, K. Yong, Appl. Catal. B: Environ. 282 (2021) 119538.
[14] N. Li, W. Wang, L. Zhu, et al., Chem. Eng. J. 421 (2021) 127857.
[15] L. Yang, Y. Xiang, F. Jia, et al., Appl. Catal. B: Environ. 292 (2021) 120198.
[16] P. Wei, S. Yin, T. Zhou, et al., Sep. Purif. Technol. 266 (2021) 118544.
[17] L. Chai, Y. Wang, N. Zhou, et al., J. Colloid Interface Sci. 581 (2021) 475–484.
[18] P. Zhang, C. Xue, Y. Li, et al., Chem. Eng. J. 404 (2021) 126497.
[19] H. Wang, B. Liao, T. Lu, Y. Ai, G. Liu, J. Hazard. Mater. 385 (2020) 121552.
[20] Y. Li, Q. Shen, R. Guan, et al., J. Mater. Chem. C 8 (3) (2020) 1025–1040.
[21] L. Li, C. Guo, J. Ning, et al., Appl. Catal. B: Environ. 293 (2021) 120203.
[22] J. Ni, W. Wang, D. Liu, et al., J. Hazard. Mater. 408 (2021) 124432.
[23] H. Yu, J. Huang, L. Jiang, et al., Chem. Eng. J. 402 (2020) 126187.
[24] B. Pan, Y. Wu, B. Rhimi, et al., J. Energy Chem. 57 (2021) 1–9.
[25] Y. Xiao, K. Wang, Z. Yang, et al., J. Hazard. Mater. 414 (2021) 125487.
[26] J. Ni, D. Liu, W. Wang, et al., Chem. Eng. J. 419 (2021) 129969.
[27] A. Wang, Q. Zhu, Z. Xing, Chem. Eng. J. 393 (2020) 124781.
[28] M.Q. Yang, C.F. Tan, W. Lu, K. Zeng, G.W. Ho, Adv. Funct. Mater. 30 (43) (2020) 2004460.
[29] W. Li, X. Wu, J. Chen, et al., Sens. Actuators B: Chem. 253 (2017) 144–155.
[30] C. Li, S. Yu, H. Che, et al., ACS Sustain. Chem. Eng. 6 (2018) 16437.
[31] K. Zhang, D. Li, Q. Tian, et al., Ceram. Int. 47 (2021) 17109.
[32] H. Cao, F. Cai, K. Yu, et al., ACS Sustain. Chem. Eng. 7 (2019) 10847.
[33] W. Shi, F. Guo, S. Yuan, Appl. Catal. B 209 (2017) 720.
[34] F. Chen, Q. Yang, Y. Wang, et al., Appl. Catal. B 205 (2017) 133.
[35] Y. Liu, L. Chen, X. Liu, et al., Chin. Chem. Lett. 33 (2022) 1385–1389.
[36] D. Huang, X. Sun, Y. Liu, et al., Chin. Chem. Lett. 32 (2021) 2787–2791.
[37] W. Liu, W. Zhang, M. Liu, et al., Chin. Chem. Lett. 30 (2019) 2177–2180.
[38] M. Cai, Z. Wu, Z. Li, et al., Nat. Energy 6 (2021) 807–814.